Surfaces and Interfaces 59 (2025) 105978

Contents lists available at ScienceDirect

Surfaces and Interfaces

journal homepage: www.sciencedirect.com/journal/surfaces-and-interfaces

Reduction of tumor burden via precise photothermal release of sirolimus by carbon nanodots in 3D plexiform neurofibroma-in-a-dish models

Marina Macchiaiolo [a,1], Roberta Cillari [b,1], Michaela V. Gonfiantini [a], Antonella Cacchione [c], Angela Mastronuzzi [c], Gennara Cavallaro [b], Davide Vecchio [a,*], Nicolò Mauro [b,*]

[a] *Rare Diseases and Medical Genetics Unit, Bambino Gesù Children's Hospital -IRCCS Rome, Italy*
[b] *Laboratory of Biocompatible Polymers, Department of "Scienze e Tecnologie Biologiche, Chimiche e Farmaceutiche" (STEBICEF), University of Palermo, Via Archirafi, 32 90123 Palermo, Italy*
[c] *Neuro-oncology Unit, Onco-haematology, Cell Therapy, Gene Therapies and Hemopoietic Transplant, Bambino Gesù Children's Hospital -IRCCS Rome, Italy*

A R T I C L E I N F O

Keywords:
Plexiform neurofibroma
Neurofibromatosis Type I
Carbon nanodots
Sirolimus
Targeted drug delivery
Photothermal therapy

A B S T R A C T

Plexiform neurofibromas (PNs) are benign but complex tumors associated with neurofibromatosis type 1 (NF1), often making surgery difficult due to hypervascularization. PNs may progress to malignant tumors, increasing mortality risks, especially in adolescence and adulthood. Personalized therapies, such as chemo-photothermal image-guided treatments, provide targeted, less invasive options, improving efficacy where surgery is not viable. Carbon nanodots (CDs) with red-to-near-infrared fluorescence and efficient photothermal conversion in the biologically transparent window (750–1100 nm) show promise as theranostic tools, enabling localized heating of cancer cells under imaging guidance. CDs can also combine photothermal therapy with light-triggered, on-demand drug release due to their large surface area and zero-dimensional size. In this study, we developed a drug-loaded CDs-based nanoplatform with a narrow size distribution (8.3 ± 0.6 nm) that is optically and colloidally stable, functionalized with biotin-PEG chains via a copper(I)-catalyzed click reaction. This CDs-PEG-BT conjugate consists of an N-doped graphitic core (~ 2 nm) functionalized with PEG2k chains bearing biotin, serving as a colloidal stabilizer and tumor-targeting agent. Additionally, the PEG shell was loaded with sirolimus (5 % w/w), a water-insoluble and unstable mTOR inhibitor effective against PNs. The drug was released in a near-infrared-sensitive manner, allowing controlled, localized release upon laser stimulation. The potential of the CDs-PEG-BT@Sir conjugate for fluorescence imaging and chemo-photothermal therapy was demonstrated both in vitro and in 3D PN-in-a-dish models, simulating the complex tumor microenvironment. The CDs-PEG-BT@Sir platform offers high colloidal and fluorescence stability, effective photothermal conversion, and selective tumor targeting, showing strong potential as a theranostic agent for precision NF1 treatment.

1. Introduction

Neurofibromatosis type 1 (NF1; MIM#162,200), is an autosomal dominant condition characterized by various combinations of multiple café-au-lait macules (CALMs), skinfold freckling, iris Lisch nodules, choroidal abnormalities, cutaneous neurofibromas (cNFs), plexiform neurofibromas (PNs), tumors of the central nervous system such as Optic Pathway Gliomas (OPG) or other Low-Grade Gliomas (LGG), osseus dysplasia and other features [1,2]. Malignancies in NF1 (PNs, malignant peripheral nerve sheath tumors (MPNSTs), female breast cancer) are the leading causes of death and impairment of the Quality of Life (QoL), reducing the average life expectancy of the patients by 8–21 years [2,3]. PNs, typically found in 50–60 % of NF1 patients, are benign nerve sheath tumors that often lead to morbidity among NF1 patients due to limited medical and/or surgical interventions [4,5]. PNs arise within nerves and consist of multiple cell types, including Schwann cells (immersed in a variably loose myxoid stroma), fibroblasts, perineural cells, mast cells, and macrophages [6,7]. PNs can progress to malignant tumors,

---

Via Archirafi 32, 90123 Palermo (Italy)Viale di San Paolo 15, 00146 Roma (Italy)
* Corresponding authors.
E-mail addresses: davide.vecchio@opbg.net (D. Vecchio), nicolo.mauro@unipa.it (N. Mauro).

[1] These authors have equally contributed to this work

https://doi.org/10.1016/j.surfin.2025.105978
Received 25 November 2024; Received in revised form 11 January 2025; Accepted 4 February 2025

specifically to malignant MPNST, increasing the risk of mortality, especially in adolescence and adulthood.

The mTOR pathway has emerged as a promising target for treating PNs, with sirolimus (Sir), an FDA-approved mTOR inhibitor, demonstrating efficacy in managing progressive PNs [8–10]. However, sirolimus pharmacokinetics present formidable challenges: its poor solubility (2.6 μg mL^{-1} at 25 °C), low and variable oral bioavailability (~14 %), and extensive distribution in the bloodstream hinder its effective delivery [9]. To overcome these limitations, various drug delivery strategies—such as nanocrystals, liposomes, and polymeric nanoparticles—have been explored [11–13]. It was also encapsulated with a near infrared (NIR)-responsive dye named indocyanine green (ICG) inside liposomes to gain image-guided chemophotothermal therapy (IG-PTT) [14]. The theranostic liposomes of 150 nm in diameter were stable and produced synergistic anticancer effects combining hyperthermia and m-TOR inhibition under the guidance of fluorescence imaging in vivo on cervical cancer models. Despite advances, there remains a need for nanosystems that simultaneously address drug solubility, stability, targeted delivery, and IG-PTT.

Recent studies have shown that elevated temperatures due to NIR-responsive nanoplatforms can enhance the release of chemotherapeutic drugs, and improve tumor cell sensitivity to chemotherapy. Consequently, the combination of PTT and chemotherapy has the potential to provide enhanced anticancer effects, addressing the limitations associated with using either therapy alone [15,16]. Carbon nanodots (CDs), zero-dimensional carbon allotropes of 1–10 nm in diameter, have emerged as promising theranostic platforms due to their high biocompatibility, optical tunability, and suitable photothermal conversion (PC > 20 %) in the NIR region [17–20]. With proper engineering, CDs can enable real-time fluorescence imaging (FLI), IG-PTT, and NIR-triggered drug release, while maintaining high dispersibility and bioeliminability *in vivo.* Surface phenomena play a pivotal role in the performance of CDs, as surface functionalization directly impacts drug loading, fluorescence properties, and colloidal stability. Interestingly, biotinylated CDs selectively target cancer cells and provide controlled, NIR-triggered drug release showcasing the importance of surface engineering in optimizing their multifunctionality [16,21–23]. Indeed, we previously demonstrated that biotinylated red-emitting CDs preferentially enter cancers cells instead of normal ones and, after irradiation with an 810 nm diode laser, they can generate heat and release their payload in a pulsed fashion inside breast cancer organoids overexpressing biotin receptors. Even if there are not available data indicating specific overexpression of biotin receptors in PNs, many studies have shown that biotin appears to play a particularly important role in neuron and human blood–brain barrier biochemistry, expressing receptors that could be targeted for therapeutic purposes [24–26].

On these grounds, we developed biotinylated CDs capable of reversibly loading sirolimus, addressing its solubility and stability challenges while maintaining optical and colloidal stability under physiological conditions. Importantly, we demonstrated that SIR adsorption does not interfere with the CDs' red fluorescence, avoiding quenching effects [27,28] often seen in optical nanomaterials and highlighting how nanoscale interactions can be leveraged to achieve high drug loading without compromising optical performance. For the first time, we hypothesized the application of biotinylated CDs as theranostic nanoplatforms for IG-PTT of PNs. Combining the photothermal effects and fluorescence imaging capabilities of CDs with the mTOR inhibition of SIR, we aimed to achieve enhanced selectivity and efficacy against PNs both on 2D and 3D models. While our study highlights the promise of IG-PTT in treating PNs, limitations remain, particularly in improving fluorescence quantum yield within the NIR-I/II window to enhance imaging and therapeutic depth. Nevertheless, our findings provide a strong foundation for advancing surface-engineered nanoplatforms and addressing the unmet needs of rare diseases like NF1-associated PNs through innovative theranostic strategies.

2. Materials and methods

2.1. Materials

Urea (99 %), citric acid (99.5 %), N,N-dimethylformamide (DMF), azide-PEG$_3$-biotin conjugate (98 %), ascorbic acid (98 %), copper (II) sulfate (CuSO$_4$, 97 %), Sirolimus (Sir, 97 %), Sephadex® G-10, G-15, and G-25, sirolimus (rapamycin, > 95 %), Transwell-COL Corning® Collagen-coated (PTFE membrane, 6.5 mm, 0.4 μm pores) inserts, ECM Gel from Engelbreth-Holm-Swarm murine sarcoma, and Dulbecco's phosphate buffered saline (DPBS) were purchased from Merck Life Science S.r.l. (Milan, Italy).

Dulbecco's Modified Eagle's Medium (DMEM), fetal bovine serum (FBS), L-glutamine (99 %), penicillin (98.5 %), streptomycin (98.5 %), and amphotericin B (98 %) were purchased from EuroClone S.p.A. (Milan, Italy).

The CellTiter 96 AQueous One Solution Cell Proliferation Assay (MTS) was purchased from Promega (Milan, Italy).

2.2. In vitro models and cell culturing

The tumoral human neurofibroma-derived Schwann cell line hTERT NF1 ipNF95.11bC (NF1) and the normal human Schwann cell line hTERT ipn02.3 2λ (HSC) (ATCC) were used as models of plexiform neurofibroma and corresponding healthy tissue respectively. Both cell lines were cultured in Dubecco's Modified Eagle's Medium (DMEM) supplemented with FBS (10 % v/v), 2 mM L-glutamine, penicillin G (100 U mL^{-1}), streptomycin (100 mg mL^{-1}), and amphotericin B (2.5 μg mL^{-1}). Cells were kept in T75 flasks at 37 °C and 5 % CO$_2$ during all the studies.

Cells employed for in vitro 2D studies were seeded on 96-well plates at a 1.5×10^4 cell per well density and cultured in DMEM for 24 h before incubating with the samples.

3D in vitro models of PNs were developed by adopting a method previously reported for breast cancer models by Mauro et al. (2019) [29] In detail, 200 μL di ECM Gel were laid in the upper chamber of a Transwell-COL Corning® (Collagen-coated PTFE membrane, 6.5 mm, 0.4 μm pores) insert, and kept at 37 °C for 10′. A suspension of NF1 cells (1.5×10^5 cells) in 300 μL of DMEM supplemented with a lower concentration of FBS (0.2 %) was added above the formed gel. The transwell inserts were placed in a 24-well plate, and the lower chamber was filled with 700 μL of complete DMEM (10 % FBS). These culturing systems were kept at 37 °C and 5 % CO$_2$, replacing the culturing medium in each chamber daily. Well-organized 3D spheroids were obtained after 4 days.

2.3. Synthesis and characterization of biotinylated carbon nanodots (CDs-PEG-BT)

Biotinylated carbon nanodots were synthesized in three steps. Briefly, plain carbon nanodots (CDs) were prepared by solvothermal decomposition of urea (6 g) and citric acid (3 g) in DMF (160 °C, 4 h). CDs were carefully purified by size exclusion chromatography (SEC), using a Sephadex® G-10/G-15/G-25 stationary phase. The obtained red-emitting CDs were freeze-dried obtaining a dark powder (Yield 43 %).

In the second step, CDs were dispersed in water (10 mL, 2 mg mL^{-1}), and amino-PEG-alkyne (H$_2$N-PEG-CC, 250 mg) was added. The pH was adjusted to 6.4, and then EDC (24.92 mg, 0.13 mmol) and NHS (14.96 mg, 0.13 mmol) were added under magnetic stirring. The reaction was kept at pH 6.4 overnight, and then the product (CDs-PEG-CC) was purified by dialysis against water and freeze-dried. Finally, CDs-PEG-CC (50 mg) and azido-PEG$_3$-biotin (53 mg) were dispersed in 4 mL of water, then ascorbic acid (10 % cat.) and copper (II) sulfate (10 % cat.) were added to the solution under nitrogen atmosphere. The reaction was kept stirring overnight, then the product (CDs-PEG-BT) was purified by QuadraPure® (15 mg) for 30 mins, and by SEC using the same stationary phase previously described, and freeze-dried.

The size distribution of CDs was assessed based on their height derived from atomic force microscopy (AFM) micrographs. AFM measurements were conducted in air using a Bruker FAST-SCAN microscope equipped with a closed-loop scanner (maximum scan ranges in X, Y, Z axes: 35, 35, 3 μm, respectively). Scans were performed in soft tapping mode utilizing a FAST-SCAN-A probe with an apical radius of approximately 5 nm, with each image resolution comparable to the tip radius. Structural analysis of CDs and CDs-PEG-BT was carried out using a JEOL JEMS-2100 high-resolution transmission electron microscope (HRTEM) operating at an electron energy of 200 kV. The samples were prepared in ultrapure water (1 mg L^{-1}) and deposited on a 400 μm mesh copper grid coated with a holey amorphous carbon film, approximately 3 nm thick. The surface functional groups of the CDs and their derivatives were investigated via Fourier transform infrared spectroscopy (FTIR) using a Bruker Alpha II spectrometer in transmission mode (24 scans, resolution: 4 cm^{-1}). Samples were prepared as KBr pellets. The pK_a values and meq of surface acidic groups were determined using the de Levie method for acid–base equilibria in polyelectrolytes (Supporting Information). All samples (30 mg) were dispersed in 0.0036 M HCl (15 mL), diluted with CO_2-free water to a total volume of 20 mL, and titrated with 0.01 M CO_2-free NaOH at 25 ± 0.1 °C under a nitrogen atmosphere, using an AMEL 631 differential electrometer. Reverse titrations were conducted with 0.01 M HCl, employing dynamic injection volumes between 0.010 and 0.100 mL. To maintain consistent H^+ ion activity, the ionic strengths of HCl and NaOH solutions were adjusted to 0.10 M by dissolving NaCl. The pH-metric system was calibrated using multiple standard buffer solutions (pH = 1, 4, 7, 9, 10, and 11), yielding a calibration fit with an R^2 of 0.9998, a slope of 56.79 mV, and an ideality coefficient of 96.4 %.

Zeta-potential values of CDs and the CDs-PEG-BT sample were measured using a Malvern Zetasizer NanoZS instrument equipped with a 633 nm laser and a scattering angle of 173°. Measurements were recorded at 25 °C, and the values obtained from the analyses were derived using the Smoluchowski equation. The samples were prepared by dispersing the powder at a concentration of 0.25 mg mL^{-1} in PBS pH 7.4.

The amount of biotin pendants was quantified by HABA/Avidin assay, following the manufacturer's instructions. In detail, 100 μL of a 0.6 mg mL^{-1} solution of CDs-PEG-BT were added to 900 μL of HABA/Avidin reconstituted reagent or to 900 μL of ultrapure water (blank), and the 500 nm absorbance of the HABA/Avidin reconstituted reagent (900μL), of the blank (1 mL), and of the mixture (1 mL) were measured. The concentration of biotin moieties was calculated as follows:

$$[BT]\ \left(mmol\ mL^{-1}\right) = \frac{\left[0.9 * Abs_{500\ (HABA\ Avidin)} + Abs_{500\ (blank)} - Abs_{500\ (mixture\ Haba\ Avidin+sample)}\right] * 10}{34}$$

2.4. Preparation and characterization of sirolimus-loaded biotinylated carbon nanodots (CDs-PEG-BT@Sir)

The incorporation of sirolimus into CDs-PEG-BT was achieved by dissolving CDs-PEG-BT (35 mg) and sirolimus (6.4 mg, 14.0 μmol) in 15 mL of chloroform and keeping the mixture stirring at room temperature for 3 days. The organic solvent was then removed by rotary evaporation, and the product was resuspended in ultrapure water (5 mL), filtered through a 5 mm syringe filter, and dialyzed against water (MWCO = 2 kDa). After 3 h, the product (CDs-PEG-BT@Sirolimus) was retrieved, and freeze-dried to obtain a dark power with a 60 % yield.

To evaluate the drug loading (DL%) capacity, 4 mg of CDs-PEG-BT@Sirolimus were dispersed in ethanol (EtOH, 10 mL) and sonicated to help the extraction of the drug (15 min 3 times). The solution was filtered and its absorbance at 277 nm was measured and compared to a calibration curve obtained by measuring the 277 nm absorbance of sirolimus standard solutions in EtOH (0.001 – 0.100 mg mL^{-1}).

2.4.1. Optical characterization of CDs-PEG-BT@Sir and parent compounds

The absorption spectra of bare CDs and CDs-PEG-BT were recorded using a double beam spectrophotometer (Shimadzu UV-2401 PC) operating in the 200–800 nm range (1 nm bandwidth) in a 1 cm quartz cuvette. The emission spectra of the bare CDs, CDs-PEG-BT, and CDs-PEG-BT@Sir were collected on diluted solutions in ultrapure water or phenol red free DMEM by a JASCO FP-6500 spectrofluorometer in a 1 cm cuvette with a 2 nm resolution bandwidth. To assess the photostability, emission quenching measurements were carried out using the same procedure above reported, but with an excitation time of 10 min.

2.4.2. Colloidal stability of the conjugates under physiological conditions

The physicochemical colloidal stability of the CDs-PEG-BT@Sir conjugate was assessed by recording the absorption spectra up to 24 h of incubation in phenol red free DMEM, and using a double beam spectrophotometer (Shimadzu UV-2401 PC) operating in the 200–800 nm range (1 nm bandwidth) in a 1 cm quartz cuvette. Samples were incubated at 37 °C in an orbital shaker (Thermo Scientific, MaxQ 420 HP, Milan, Italy) at 100 rpm for 24 h, and then spectra were recorder each 1h.

2.5. Sirolimus release kinetics from CDs-PEG-BT@Sirolimus

The release profile was obtained in PBS pH 7.4 and 0.1 % w/v Brij58 using the dialysis method. Sirolimus (10 μg), or an equivalent amount of CDs-PEG-BT@Sirolimus, was dissolved in 4 mL of fresh medium and placed inside a dialysis test tube with nominal molecular weight cut off (MWCO) 1 kDa. Then, the test tube was immersed in 16 mL of medium and incubated in an orbital shaker (Thermo Scientific, MaxQ 420 HP, Milan, Italy) at 100 rpm, 37 °C for 48 h. The sampling points were set up as 1 h, 3 h, 5 h, 6 h, 8 h, 12 h, 24 h, and 48h. At each sampling time, 0.5 mL of release medium was retrieved, substituted with fresh medium, and analyzed using HPLC (Agilent Infinity 1200, C6-phenyl column) with acetonitrile/H_2O 70:30 as eluant (0.8 mL min^{-1}) and a UV–Vis diode detector at 277 nm. All the release experiments were repeated three times to report the mean ±s.d..

2.6. In vitro cytotoxicity study on a 2D model

The cytotoxic effect of CDs-PEG-BT@Sirolimus was first evaluated on an *in vitro* 2D model by MTS assay. For the 2D experimental set, HSC or NF1 cells were seeded on a 96-well plate at a 1.5 × 10^4 cells per well density and incubated for 24 h at 37 °C and 5 % CO_2. The culture medium was then removed and cells were treated with 150 μL of either free sirolimus in DMEM (150 – 10 μg mL^{-1}) or equivalent amount of CDs-PEG-BT@Sirolimus. Negative controls were incubated with 150 μL of fresh medium. After 24 h, the culture medium was withdrawn and cells were washed twice with DPBS. To perform the cell viability assay, every well was treated with 120 μL of MTS working solution, which was prepared by diluting the MTS stock solution with DMEM (1:6). After 2 h of incubation, the 492 nm absorbance of the samples was measured using a microplate reader (Multiskan, Thermo, UK), and compared with the absorbance of negative controls, assumed as 100 % of cell viability. The experiment was performed in triplicate.

2.7. Evaluation of the cytotoxic effect of CDs-PEG-BT@Sirolimus treatment on a 3D-model of plexiform neurofibroma

A 3D model of plexiform neurofibroma was obtained by preparing NF1 spheroids in a culturing system consisting of an ECM Gel layer, formed above the membrane of Transwell-COL Corning® inserts (Collagen-coated PTFE membrane, 6.5 mm, 0.4 μm pores), on which cells were cultured in presence of a FBS gradient (0.2 – 10 % FBS) for 4 days. After this period, the culturing medium in the upper chamber was replaced with 200 μL of CDs-PEG-BT@Sirolimus (1.36 mg mL^{-1}) or free sirolimus (23 μg mL^{-1}) in DMEM supplemented with 0.2 % of FBS. While, fresh medium was added to the controls. Then, spheroids were incubated for seven days, changing the upper medium each three days, to evaluate cell viability and volume progression.

The photothermal effect induced by NIR-irradiation of CDs-PEG-BT@Sirolimus was assessed in a parallel experimental set. Spheroids, prepared and treated as previously described, were also irradiated with an 810 nm diode laser (GBox 15A/B diode, GIGAA laser, 7 W cm^{-2} power density, 300 s) on day 3 and culture for additional four days to follow the growth trend up to seven days.

For both the experimental sets, the spheroids' size was monitored at scheduled time intervals (day 0 - day 7) using an optical microscope equipped with an Axio Cam MRm (Zeiss) digital camera.

For NF1 spheroid viability analysis, an MTS assay (CellTiter 96 AQueous One Solution Cell Proliferation Assay, Promega) was performed each day. In detail, spheroids were removed, placed into a 96-weel plate, and incubated with the MTS solution (200 μL) for 3h. Then, cell viability was calculated from the 492 nm absorbance of the samples measured using a microplate reader (Multiskan, Thermo, UK), and compared results with the absorbance of negative controls, assumed as 100 % of cell viability.

On day 3 NIR-treated spheroids were stained using a Live/Dead Cell Double Staining Kit, following the manufacturer's instructions. Briefly, the culture medium was removed from the upper chamber and it was washed twice with DPBS. Spheroids were then incubated with a live/dead working solution, prepared by adding 5 mL of solution B, and 10 mL of solution A to 5 mL of PBS, for 15′. Spheroids were then washed twice with PBS and fixed with 4 % buffered formalin. Micrographs were acquired using a widefield fluorescence microscope equipped with an Axio Cam MRm (Zeiss).

All independent experiments were performed in triplicates.

2.8. Cellular uptake of CDs-PEG-BT@Sirolimus

The self-fluorescence of CDs-PEG-BT in the red region was exploited to evaluate the cellular internalization of CDs-PEG-BT@Sirolimus on 2D HSC or NF1 cell lines, and on the established 3D model. In detail, for the 2D cell uptake study cells (NF1 or HSC) were seeded in glass chamber coverslip at a density of 5×10^3 cells per well and grown in DMEM. After 24 h, the medium was replaced with 200 μL of fresh culture medium containing CDs-PEG-BT@Sir (0.1 mg mL^{-1}) and cells were incubated for 6h. The 2D cell uptake of CDs-PEG-BT was evaluated by fluorescence microscopy recording red fluorescence (TxR channel) micrographs by an Axio Cam MRm (Zeiss). Untreated cells were used as negative control to set up the autofluorescence. The amount of relative fluorescence per cell was extrapolated by imageJ software, considering the average area of fluorescence intensity obtained from the red channel of at least six different cells. For the spheroids were prepared and treated with CDs-PEG-BT@Sirolimus as previously described, maintaining the same treatment schedule adopted for the evaluation of their cytotoxic effect. On day 7 (t_3), the culture medium of the upper chamber was removed and spheroids were washed twice with DPBS. Micrographs of the spheroids were acquired using a widefield fluorescence microscope equipped with an Axio Cam MRm (Zeiss).

2.9. Statistical analysis

Statistical analysis was performed using the Student's T-test (two-tailed). Statistical calculations were performed using the Microsoft®-Excel data analysis tool and the software package GraphPad Prism (V.7.03). Comparisons were considered statistically significant at $p < 0.05$ (*), $p < 0.01$ (**), and $p < 0.001$ (***).

3. Results and discussion

3.1. Synthesis and physicochemical characterization of the CDs-PEG-BT

The red-emitting carbon dot core (CDs) was obtained following a procedure reported elsewhere, with modifications [16]. In detail, CDs were synthesized by the solvothermal decomposition of citric acid and urea, serving as oxygen and nitrogen donors, respectively, in DMF at 160 °C under 8 atmospheres of pressure.

The pressure plateau was reached after 1 h, attributed to the release of decomposition gases such as CO, CO_2, dimethylamine, and NH_3. The reaction workup involved the removal of the reaction solvent under vacuum, the redispersion of the dark powder in ultrapure water, and the isolation of red-emitting CDs by size exclusion chromatography (SEC), The purification procedure was performed using a column packed with a combination of Sephadex® stationary phases with decreasing cutoff values (G-10 → G-15 → G-25), chosen on the basis of previous works, and water as eluant [19].

After freeze-drying, we obtained a reddish dark powder which consists of crystalline CDs of 1.6 ± 0.3 nm in diameter (Fig. 1a-a'), with narrow size distribution (Figure 1a'-b) and crystalline lattice fringes with a spacing of 2.252 Å (Fig. 1a), and endowed with a bright emission from the green (19 %) to the red region (QY 5.3 %) (Figure S1a). Although CDs with higher quantum yields (QY) in the red region (9 % - 18 %) have been reported, the CDs synthesized in this work possess a QY suitable for in vivo bioimaging applications [30,31]. Additionally, they were produced on a gram scale (43 % yield—one of the highest reported), with high homogeneity, indicating that the proposed protocol is robust and suitable for real-world applications [19]. It is worth noting that CDs are typically synthesized with very low reaction yields, which often limits their potential applications [32–34]. As shown in Fig. 3a, the obtained CDs are characterized by the presence of several polar groups such as OH, $CONH_2$ and COOH functions, amenable to further chemical functionalization. Indeed, the FTIR spectrum of bare CDs is characterized by many diagnostic vibrations of such groups, such as, for instance, those relative to OH stretching (3420 cm^{-1}), asymmetric (1711 cm^{-1}) and symmetric (1398 cm^{-1}) COOH stretching, and the amide I band (1620 cm^{-1}).

These COOH surface groups were exploited for the surface engineering with biotinylated PEG chains so as to increase the average diameter beyond the renal cutoff (5.6 nm), thus preventing the eventual rapid excretion following their in vivo administration, and actively target high proliferating cells, such as NF1, which overexpress biotin membrane receptors [21–23]. It might be expected that PEGylation with discrete chains ($\overline{M}_w = 2$ kDa) would improve the bioavailability avoiding protein corona adsorption and opsonization [35]. Hence, we conjugated biotinylated PEG_{2000} chains through a step-by-step surface conjugation procedure. First of all, CDs were functionalized with amino-PEG-alkyne (NH_2-PEG-CC) chains obtained as previously described (Supplementary; Fig. S2–4) [21]. Briefly, NH_2-PEG-CC was coupled to the CD's carboxyl functions using EDC and NHS as coupling agents under slightly acidic conditions. Then, biotin pendants were conjugated at the alkyne end-chain on the CDs surface by the Cu (I)-catalyzed azide-alkyne Huisgen dipolar cycloaddition (Fig. 2), employed to quantitively convert the alkyne groups of PEG chains into 1,3-triazole using azido-PEG_3-biotin moieties. The catalyst was removed by means of the resin QuadraPure® before performing the final

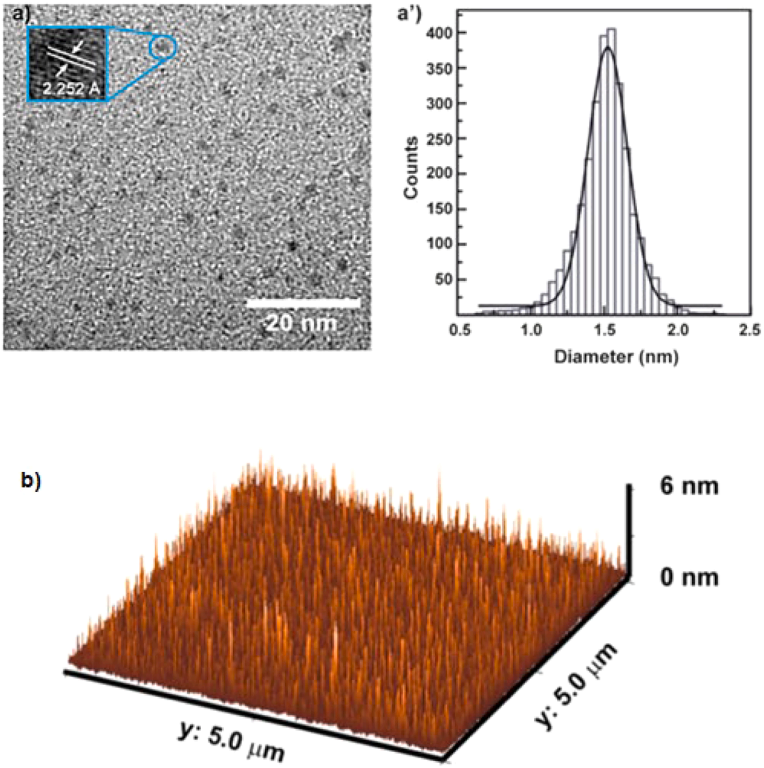

Fig. 1. High-resolution transmission electron microscope (HRTEM) micrograph of bare CDs (a), obtained by a JEOL JEMS-2100 operating at 200 kV electron energy: analysis of size distribution based on AFM data (a'). Atomic force microscopy (AFM) micrograph of bare CDs obtained on MICA using a Bruker FAST-SCAN microscope equipped with a closed-loop scanner (X, Y, Z maximum scan regions: 35, 35, 3 µm, respectively).

purification step by SEC. The final surface engineering with PEG-BT chains was confirmed by combining complementary techniques such as FTIR and De Levie titration of surface carboxyl groups. From the analysis of the FTIR spectrum of the CDs-PEG-BT conjugate it is possible to highlight the presence of characteristic vibrations of the PEG pendants at 2870 cm^{-1} (ν C—H) and 1117 cm^{-1} (ν C—O), along with an increase in vibrations typically associated to amide function at 1620 cm^{-1} (ν H−N−C = O). Additionally, a sharp decrease is observed in the symmetric (1711 cm^{-1}, ν C = O) and asymmetric (1389 cm^{-1}, ν O−C = O) vibrations of the carboxyl groups. Overall, these results suggest the conversion of carboxyl groups into amide bonds through the coupling of PEG chains. This was further confirmed by the analysis of the potentiometric titration curves obtained for the CDs-PEG-BT conjugate compared with the bare CDs (Fig. 3b).

The model adopted for the calculation of the pK_a values and equivalents of COOH surface groups is reported in Supporting information. It is self-evident that although the nature of the surface functions was preserved – the pK_a values of COOH groups remain similar before and after conjugation - the amount of carboxyl functions in CDs-PEG-BT drastically decreases after the conjugation process (from 6.7 to 1.48 meq g^{-1} for the bare CDs and the CDs-PEG-BT, respectively) (Fig. 3b) due to the coupling reaction between carboxylic acids on the CDs surface and amine end-chain of NH_2-PEG-CC (Fig. 2). The amount of biotin linked to the CDs surface was finally measured spectrophotometrically by the HABA/avidin assay, yielding 0.248 µmol mg^{-1}, equivalent to 15 biotin moieties per carbon dot.

From a chemical standpoint, using this method, surface engineering was achieved in a layer-by-layer orthogonal manner, effectively preventing dot-to-dot cross-linking by avoiding reactions with carboxylic acid groups on adjacent nanoparticles. This was demonstrated by the structural analysis of the CDs-PEG-BT conjugate through HRTEM micrographs (Fig. 3c-c'''). The size distribution of the conjugate passed from 1.6 nm to 8.3 ± 0.6 nm (Fig. 3c), corroborating the above reported data which suggests the effective conjugation of CDs with PEG chains of roughly 3 nm in hydrodynamic diameter ($\overline{M}_w =$ 2.2 kDa). HRTEM showed that the crystalline nature of the CDs core is preserved in CDs-PEG-BT after the surface engineering procedure. Indeed, the lattice fringe reveals a graphitic carbonaceous structure with a D-spacing of 2.258 Å (Fig. 3c'-c'''). Overall, the data support the hypothesis that the surface engineering of CDs involved only the carboxyl groups on the surface and one end of the heterobifunctional PEG chains. This resulted in well-structured and homogeneous biotinylated nanoparticles with a size distribution exceeding the renal cutoff, making them potentially suitable for prolonged blood circulation [35,36]. The surface charge of the conjugate is an important parameter to establish biocompatibility and potential positive interactions with proteins, cells, and tissues *in vivo*. Thus, the Zeta-potential value of the CDs-PEG-BT conjugate was measured and compare with parent compounds. It is interesting to notice that, after surface conjugation exploiting COOH groups on the CDs surface, according to titration data reported in Fig. 3b, the Zeta-potential passed from −31.4 ± 1.7 mV to −15.4 ± 2.2 mV. This drastic reduction in the surface charge, apart from confirming the surface conjugation process observed with other techniques, implies a higher potential of the conjugate of favorably interacting with cell membranes during cell uptake processes usually occurred at the cell-nanoparticle interface.

3.2. Optical characterization of the CDs-PEG-BT and parent compounds

The CDs-PEG-BT conjugate exhibits the typical intricate optical absorption spectrum of bare CDs, which predominate over the absorption bands of PEG chains at 240 nm (Fig. 4a). In particular, there are many discrete absorption bands within the UV–visible range (340, 400, and 550 nm) which are responsible for three emission bands peaking in blue, green, and red (Fig. 4a and S1a-a').

However, surface engineering of the CDs' polar groups with PEG

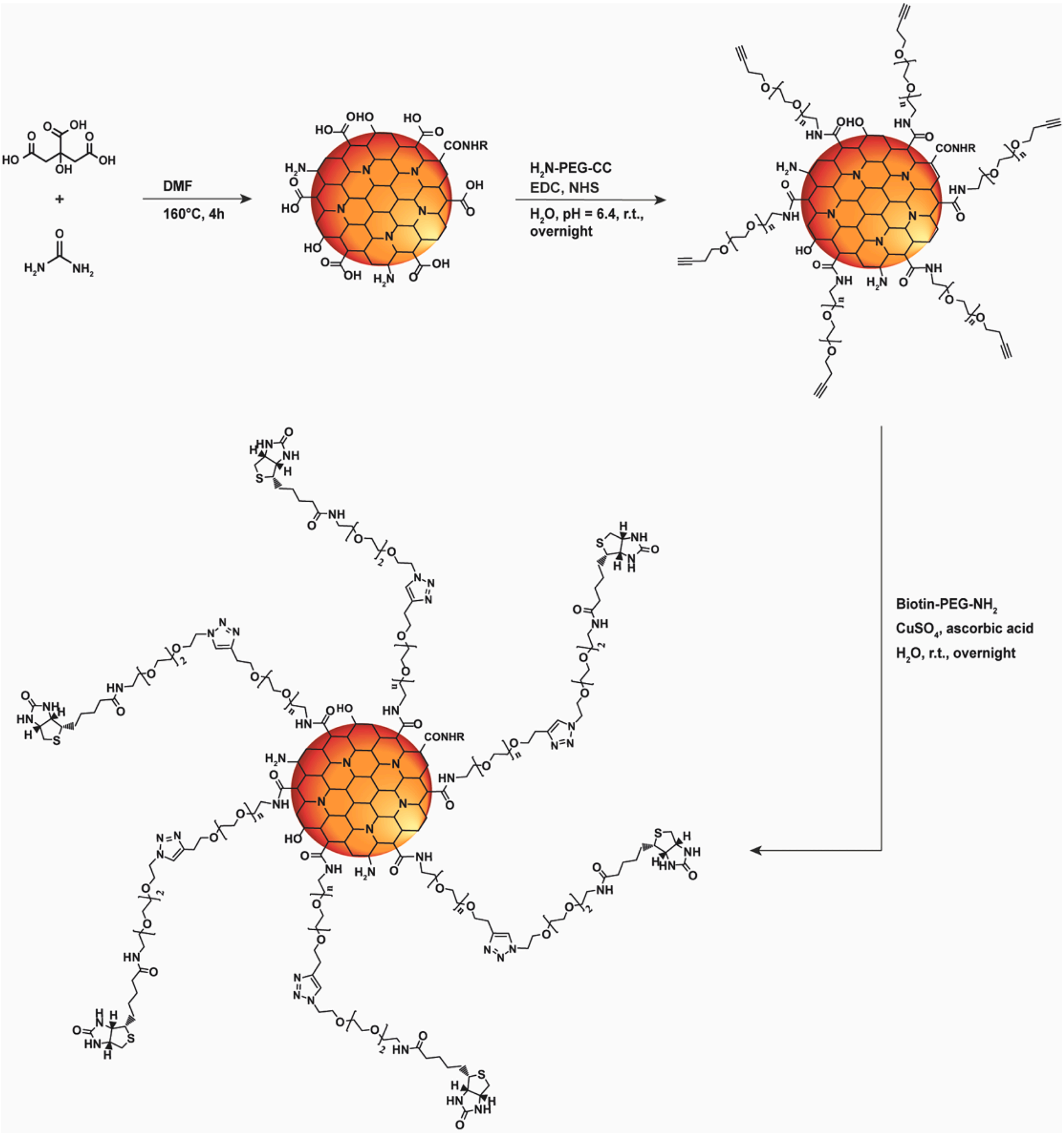

Fig. 2. Scheme of the reaction pathway adopted for the synthesis of the CDs-PEG-BT conjugate.

chains results in partial quenching of the blue and green emission bands (Figure S1a-a', Fig. 4b) and an auxochromic shift of the red emission band. This further confirms the involvement of covalent conjugation with the CDs' COOH groups and the importance of the emissive surface trap mechanism in the electronic transitions [37]. The red fluorescence stability of the CDs-PEG-BT conjugate under physiological conditions and continuous stimulation was assessed in DMEM at 37 °C after 10 min of irradiation (Fig. 4c). Unlike other optically active nanoplatforms or organic probes that undergo photobleaching upon laser excitation for bioimaging [27], CDs exhibited no reduction in fluorescence intensity even after 10 min of continuous excitation, indicating stable fluorescence over time. The importance of surface engineering of CDs is not limited to optical stability benefits, but also provides extremely high colloidal stability in DMEM. As shown in Fig. 4d, the absorption of the CDs-PEG-BT sample was stable in DMEM up to 24 h of incubation under physiological conditions, indicating that the conjugate displays high colloidal stability also in the presence of proteins and salts. It might be noticed that fluorescence stability of CDs-PEG-BT is also preserved after 24 h of incubation in DMEM under physiological conditions (Fig. 4e-e'). A similar behavior was observed after drug loading via surface adsorption on the CDs-PEG-BT@Sir surface. No differences were detected in terms of photobleaching, physicochemical stability, or optical stability following incubation of CDs-PEG-BT@Sir in DMEM. This suggests that the PEG shell not only ensures efficient drug loading, but also separates

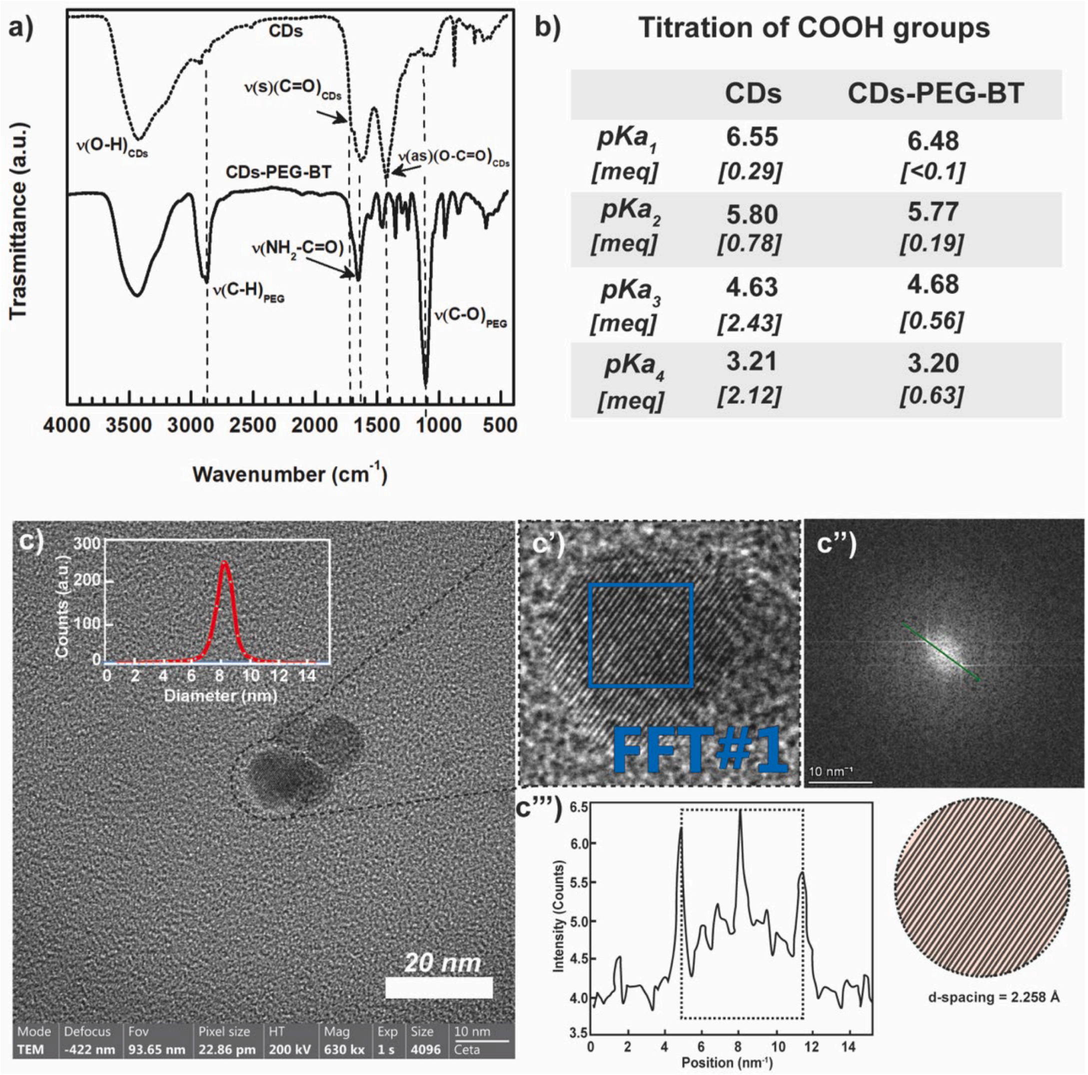

Fig. 3. Chemical and structural characterization of the CDs-PEG-BT conjugate and parent compounds. a) FTIR spectra of bare CDs compared to the conjugate performed on dried KBr pellets at a sample concentration of 1 %. b) pK_a values and meq COOH surface groups of CDs and CDs-PEG-BT calculated by the De Levie titration method (See Supplementary). c-c') Transmission electron microscopy (TEM) and size distribution (Figure insert) of CDs-PEG-BT; Fourier transform (FFT) (C'-C''') and D-spacing distribution of the CDs-PEG-BT crystalline core (Figure insert).

the adsorbed drug molecules from the surface electrons of the CDs which are responsible for the fluorescence mechanisms of the CDs' core. This findings highlights that PEGylation is a powerful and simple strategy offering a dual advantage for CDs surface engineering in theranostics.

The CDs-PEG-BT conjugate has interesting photothermal conversion under excitation with an 810 nm diode laser, allowing a temperature increment up to 20 °C at a concentration of 0.1 mg mL^{-1} and at low power density (2 W cm^{-2}) (Fig. 5a). While, ultrapure water undergoes a slight temperature increase (2 °C) under the same conditions. The NIR photothermal conversion exhibited by CDs-PEG-BT is likely derived from the long-wavelength tail of their absorption profile (Fig. 3a) and scattering phenomena, and was calculated to be roughly 21 % [16]. It was comparable to that observed for other carbon-based structures, such as mesoporous carbon nanospheres (35 %) and graphene-based nanosystems (39 %) [38,39], or optical active polymers such as polydopamine (32 %) [39]. The slightly lower photothermal conversion in emitting CDs, although suitable for PTT, arises from the inherent competition between radiative emission, which releases energy as light, and non-radiative thermal phenomena, which dissipate energy as heat.

Notably, the conjugate exhibits tunablity dependent on exposure time. This behavior allows achieving the minimum temperature of 42 °C required for tumor eradication though hyperthermia, positioning them as promising candidates as nanoheaters in image-guided photothermal therapy (IG-PTT) for cancer [40,41]. This remarkable photothermal behavior was maintained also after the drug loading process in the CDs-PEG-BT@Sir sample, reaching only an inflection of 3 °C after the same exposure conditions (Fig. 5a). Importantly, CDs are able to maintain their chemical characteristics up to 180 C°, thus implying a high thermal stability under NIR photothermal conversion [42].

3.3. Preparation and characterization of the sirolimus-loaded CDs-PEG-BT (CDs-PEG-BT@Sir)

Sirolimus is a mTOR inhibitor with IC$_{50}$ of approximately 0.1 nM in HEK293 cell lines that, being a macrolide compound with hydrophobic features, exhibit poor solubility in water (2.6 μg mL^{-1}) [43]. Besides, sirolimus has a carboxylic lactone-lactam function and many unsaturation which make it unstable under physiological conditions and, thus, requires targeted delivery to successfully exert its action in tumors. Here, we entrapped sirolimus within the polymeric shell of the CDs, as its solubility in PEG exceeded 30 mg mL^{-1}. It is also expected that sirolimus could interact with residual polar groups on the CDs' surface

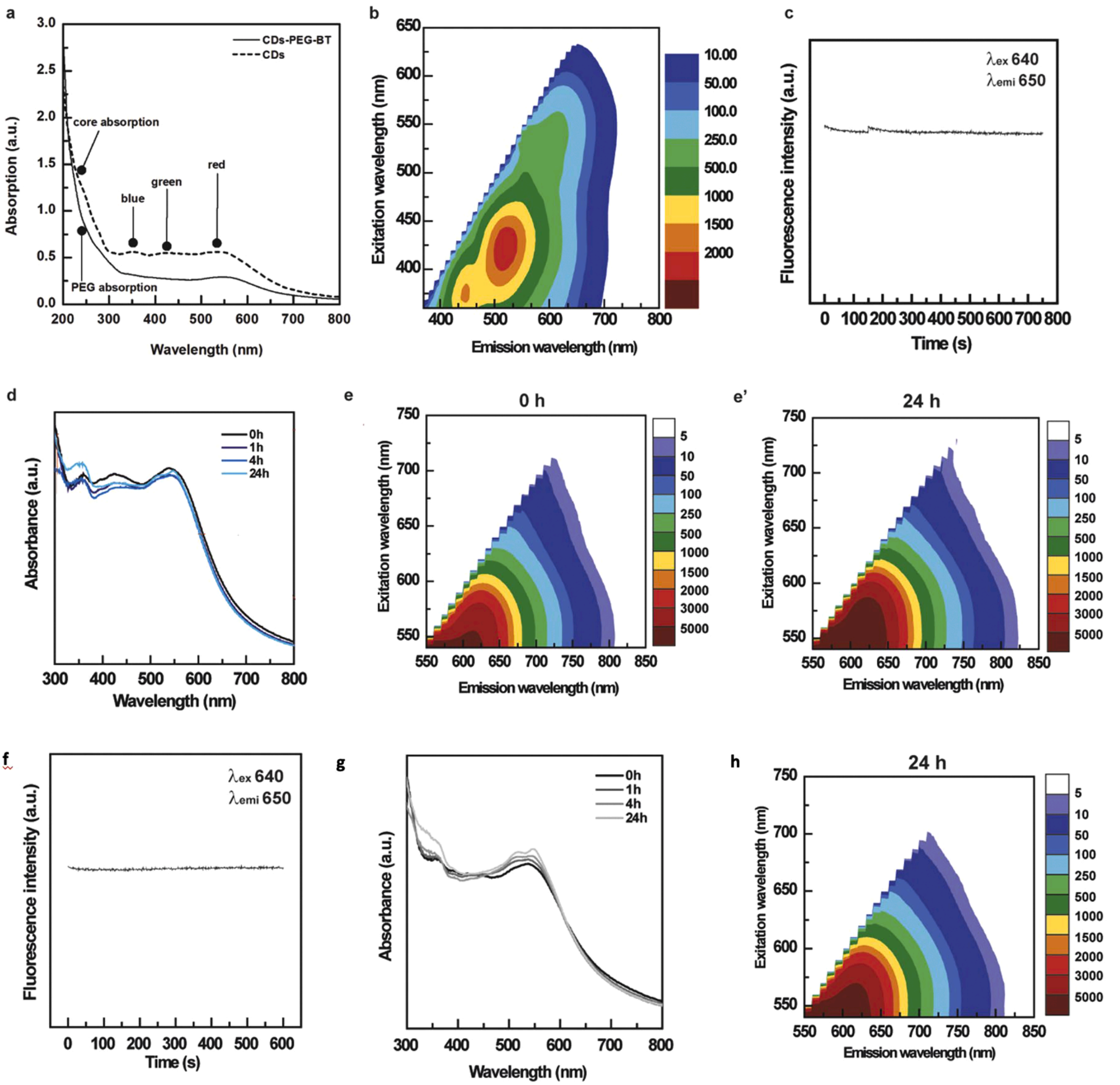

Fig. 4. Optical characterization of the CDs-PEG-BT conjugate (0.1 mg mL^{-1}): absorption **(a)** and 3D emission **(b)** spectra in water. Physicochemical and optical stability of the CDs-PEG-BT conjugate (0.1 mg mL^{-1}) in DMEM **(c-e')**: emission intensity quenching study under continuous red-light excitation for 10 mins **(c)**; UV–vis spectra kinetics up to 24 h of incubation at 37 °C **(d)**; 3D emission spectra up to after 24 h of incubation at 37 °C **(e-e')**. Physicochemical and optical stability of the CDs-PEG-BT@Sir sample (0.1 mg mL^{-1}) in DMEM **(f-h)**: emission intensity quenching study under continuous red-light excitation for 10 mins **(f)**; UV–vis spectra kinetics up to 24 h of incubation at 37 °C **(g)**; 3D emission spectra after 24 h of incubation at 37 °C **(h)**.

through hydroxyl functionalities. This was achieved by the thin-film method in chloroform and filtration of the rehydrated colloidal dispersion through a 5 μm syringe filter. The obtained sirolimus-loaded conjugate, herewith named CDs-PEG-BT@Sir, contains 4.77 % of the drug (32 % encapsulation efficiency). The drug loading reached is suitable for pharmaceutical applications in cancer therapy, as sirolimus, due to its extremely high potency, exerts pharmacological effects at nM concentrations [43,44].

Although these values are lower compared with hydrophobic polyester-based nanoparticles (~5 % vs ~13 %) [44], in principle, the higher dispersibility in aqueous media might ensure optimized therapeutic conditions in terms of dosage and bioavailability.

The drug release ability of the CDs-PEG-BT@Sir conjugate was studied in phosphate-buffered saline (PBS) at pH 7.4, both with and without exposure to an 810 nm laser diode, and compared to the dissolution profile of the free drug in the same medium. The laser exposure was used as a stimulus to induce pulsed, on-demand drug release. As shown in Fig. 5b, sirolimus was released in a controlled manner without alteration, mainly due to the protection by Brij58 micelles formed in the release medium, and without hinting at a burst effect. In particular, the conjugate released only 8 % of sirolimus after 2 h, reaching approximately 40 % release over 10 h, and plateauing at around 44 % after 22 h of incubation. Then, the release slowly proceeds during the last 26h. A similar release profile was achieved under NIR laser irradiation for 300 s, but with a 20 % increase in drug release over 48 h (Fig. 5b). Notably, the CDs-PEG-BT@Sir sample released 40 % of its

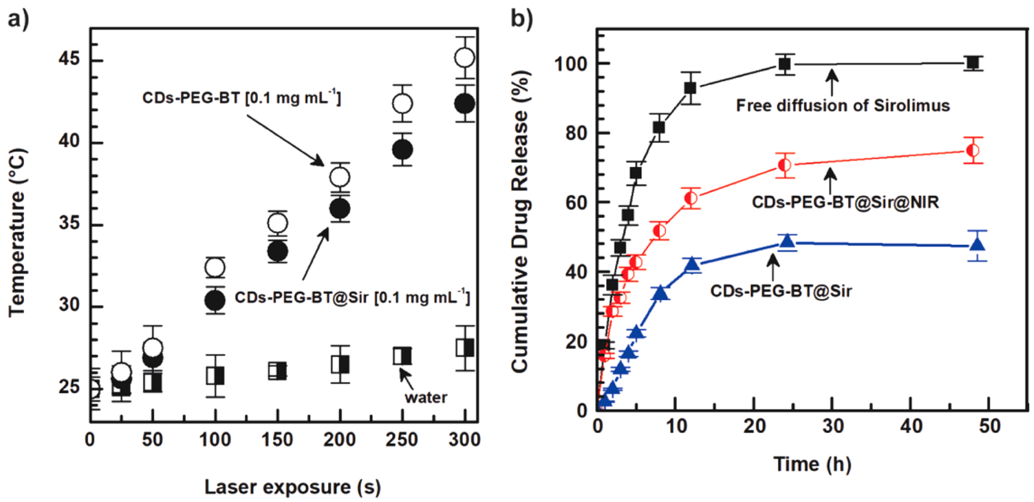

Fig. 5. Photothermal kinetics **(a)** and light-triggered drug release profile **(b)** of the CDs-PEG-BT@Sir conjugate and parent compounds.

payload within 3 h following NIR light exposure, demonstrating the feasibility of light-triggered spatiotemporal pulsed drug release. The ultrasmall size of the conjugate (d < 10 nm), along with its consequent high diffusion coefficient across the complex and dense tumor microenvironment, combined with its unique fluoresce and on-demand drug release profile, supports the potential of the developed conjugate as a candidate for selectively delivering sirolimus within tumors via image-guided photothermal therapy (IG-PTT) [20,45–48].

3.4. Biological characterization of the CDs-PEG-BT@Sir and parent compounds

Schwann cells are critical components of the peripheral nervous system. Plexiform neurofibromas arise from aberrant Schwann cell proliferation, with the latter being a hallmark of plexiform neurofibromas (PNs) [49]. These cells recapitulate key molecular and cellular features of plexiform neurofibromas, including the expression of relevant markers, growth patterns, and interactions with the tumor microenvironment. As such, Schwann cells from PNs (NF1) provide a reliable and biologically relevant model to study the pathogenesis of plexiform neurofibromas and to test potential therapeutic strategies [50]. Therefore, in the present study, the effectiveness of potential treatments using CDs-PEG-BT@Sir was studied in both 2D and 3D NF1 culture models so as to capture not only cellular responses but also the complex spatial and structural interactions present in the tumor microenvironment. These complementary approaches provide a more comprehensive evaluation of pharmacological efficacy and the potential translation into clinical practice [49,51].

3.4.1. Cytotoxicity study and cell uptake of the CDs-PEG-BT@Sir conjugate on 2-D plexiform neurofibroma (NF1) and Human Swan Cells (HSC) lines

To prove the ability of CDs-PEG-BT of acting as multifunctional nanotools for fluorescence imaging, IG-PTT, and targeted drug delivery system towards plexiform neurofibroma, we carried out preliminary experiments on 2D cell cultures. In the first step, the cytocompatibility of the CDs-PEG-BT conjugate was established on both normal (HSC) and cancer (NF1) Schwann cell lines, showing complete cytocompatibility (cell viability > 98 %) in both cases at concentrations up to 2 mg mL^{-1} (data not shown). Thus, the toxicity profile of the sirolimus-loaded conjugate, namely CDs-PEG-BT@Sir, was attained on the same 2D cultures at drug concentration ranging from 10 to 150 µg mL^{-1}, corresponding to 0.2 to 3 mg mL^{-1} in CDs-PEG-BT@Sir, respectively. Fig. 6a shows that the CDs-PEG-BT@Sir sample is cytocompatible in normal HSC cells within the entire concentration range tested, while free sirolimus provides complete cell death at concentration higher than 50 µg mL^{-1}.

Conversely, CDs-PEG-BT@Sir give rise to significant cytotoxicity phenomena (cell viability < 70 %) at concentrations higher than 50 µg mL^{-1} in cancer cells (Fig. 6b), suggesting a selective anticancer effect toward the NF1 cell line. This is corroborated by the analysis of the half minimal inhibitory concentration (IC_{50}) values obtained for HSC and NF1 cells after 24 h incubation (Fig. 6a-b). The IC_{50} value obtained for the free drug on HSC cells is comparable to that established for NF1 cancer cells, even though lower for the NF1 cells (23 vs 38 µg mL^{-1}). While, the IC_{50} calculated for the CDs-PEG-BT@Sir on NF1 cancer cells is at least three times lower with respect with normal Schwann cells (56 vs <150 µg mL^{-1}). It is interesting to notice that CDs-PEG-BT@Sir show selective cytotoxicity in cancer cells which is plausibly due to the targeted delivery at cellular level.

With the aim of assessing preferential cell uptake in NF1 cells, the CDs-PEG-BT conjugate was incubated with either NF1 or HSC cell lines at a concentration of 100 µg mL^{-1} for 6 h, and the ability of entering cells was assessed by fluorescence microscopy measuring the self-red fluorescence of the conjugate (Figure S5). As expected, CDs-PEG-BT was able of entering both healthy HSC and cancer NF1 cells, with a significantly higher fluorescence observed for the NF1 cell line.

3.4.2. Evaluation of the anticancer potential of the CDs-PEG-BT@Sir conjugate on 3-D plexiform-on-a-dish models

While 2D culture systems have significantly advanced our understanding of cellular molecular mechanisms, they fail to capture the full complexity of the tumor microenvironment, including multiple cell-cell/cell-matrix interactions found in human tissues. As a result, there is a growing recognition that 3D models, such as "plexiform neurofibroma-in-a-dish" systems, offer a more accurate pathomimetic representation of tumor biology, providing superior insights into disease mechanisms and potential therapeutic responses [52–54]. Here, we developed and studied 3D NF1- in-a-dish spheroids of 1–1.8 mm in diameter so as to establish the potential of CDs-PEG-BT@Sir as photothermal agents for targeted non-invasive treatment of plexiform neurofibroma. We treated NF1 spheroids embedded in a complex collagen matrix with either CDs-PEG-BT@Sir (with and without an 810 nm diode laser exposure) or the free drug at the IC_{50} and monitored the growth kinetics by measuring spheroid volume over time, up to 7 days of incubation. The volume progression kinetics measured by optical imaging are reported in Fig. 6c, and show that the untreated spheroids increased their volume over time, passing from 1.5 to 1.8 mm^3 after 7 days of culturing. While, NF1 spheroids treated with CDs-PEG-BT@Sir or an equivalent amount of free drug decreased their volume in a time-dependent fashion passing from 1.55 to 1.25 mm^3 in 7 days of

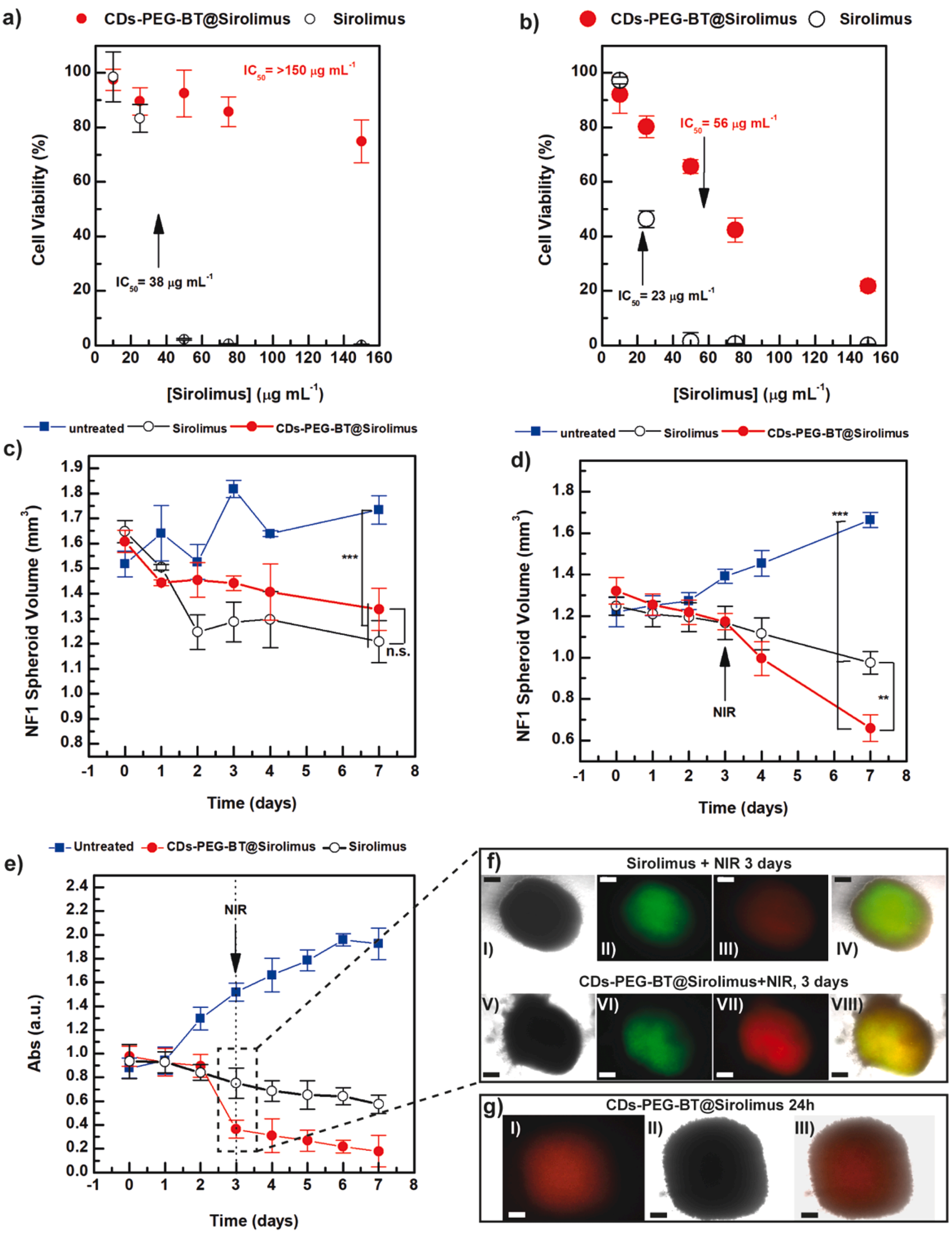

Fig. 6. MTS assay on human Schwann (HSC) **(a)** and plexiform neurofibroma (NF1) cell lines **(b)** obtained after 24 h incubation with increasing concentrations of CDs-PEG-BT@Sir or equivalent amount of free sirolimus. Progression of NF1 spheroid volume after 7 days of incubation with either the CDs-PEG-BT@Sir conjugate or free drug **(c)**, also coupled with an 810 nm diode laser exposure at 7 W cm^{-2} for 300 ss **(d)**. Cell viability by MTS assay of NF1 spheroids treated with an 810 nm diode laser exposure at 7 W cm^{-2} for 300 ss **(e)**. Live&Dead analysis of NIR treated NF1 spheroids (day 3) by fluorescence microscopy **(f I-VII)**: green (live), red (dead) cells. Cell uptake on NF1 spheroids obtained by fluorescence microscopy: red fluorescence (CDs-PEG-BT@Sir), brightfield, and merge **(g I-III)**. Magnification 5x, scalebar 0.2 mm.

incubation.

The same experiments were conducted by applying a NIR light laser exposure (7 W cm^{-2}) for 300 s in order to assess the effects of combined chemo-photothermal treatment on complex 3-D NF1 models (Fig. 6d-e). In particular, photothermal stress was applied after 3 days of incubation, thus inducing pulsed and massive sirolimus delivery as well as local hyperthermia (Fig. 5a-b). Spheroid volume and viability were then assessed by combining optical imaging (Fig. 6d) and the MTS assay (Fig. 6e). As shown in Fig. 4d, the NIR light exposure alone did not significantly affect spheroid growth over time, with spheroid volume doubling after 7 days of incubation. This means that the power density adopted was definitely biocompatible. Spheroids incubated with free sirolimus and NIR light followed the same trend of the free drug alone, passing from 1.3 to 1.0 mm^3, thus implying that NIR laser exposure did not impinge on the sirolimus pharmacological effects. Conversely, spheroids treated with CDs-PEG-BT@Sir exhibited a significant reduction in volume following NIR light exposure (from 1.16 to 0.7 mm^3), indicating that the combined chemo-photothermal treatment can synergistically induce cell death, even in complex 3D models. This was further corroborated by the cell viability assay shown in Fig. 6e, where similar trends were observed. However, it is noteworthy that the residual cell viability of spheroids treated with CDs-PEG-BT@Sir and NIR light dropped to <15 % compared to the initial viability conditions. This was further studied by the live&dead assay after the chemo-photothermal insult (3 days) both for spheroids incubated with free sirolimus and the CDs-PEG-BT@Sir conjugate. The live&dead assay was performed by fluorescence imaging subtracting the self-fluorescence of the conjugate in the green/red region (Fig. 6f). It is worth noting that the red fluorescence (indicating dead cells) in NF1 spheroids treated with the free drug was lower compared to spheroids treated with the conjugate under light exposure, while the green fluorescence, corresponding to live cells, was higher. This confirms the crucial role of the conjugate in inducing cell death by converting NIR light into heat and selectively releasing sirolimus in situ. Unfortunately, the lack of control experiments with HSC spheroids, due to the absence of conditions that produce homogeneous, reproducible, and well-structured 3D cultures, does not provide valuable insights into the selectivity of the PTT in vitro. This would require further investigations, allowing a more comprehensive evaluation of its behavior in physiologically relevant 3D microenvironments.

Finally, the ability of the CDs-PEG-BT@Sir conjugate of acting as a contrast agent in fluorescence imaging was investigated on 3-D NF1 spheroids using fluorescence imaging (Fig. 6g). Fluorescence micrographs obtained after 24 h of incubation revealed that the conjugate efficiently penetrated the spheroids, also inside the highly dense core, enabling monitoring within the biological transparency window of 620–750 nm. The efficient diffusion observed can be explained by the extremely low diameter of the CDs-PEG-BT@Sir conjugate (~ 8 nm) which allows for rapid diffusion throughout the well-structured NF1 mass. Typically, nanomedicines with larger dimensions (20–100 nm) can extravasate from the bloodstream to reach the tumor stroma. However, their diffusion within the tumor parenchyma is often restricted due to the low permeability of the highly dense collagen matrix in the tumor microenvironment [55–57]. Overall, the ultrasmall size distribution of the CDs-PEG-BT@Sir conjugate, combined with bright fluorescence imaging contrast, light-responsive hyperthermia, and on-demand drug release, represents an ideal combination for effective image-guided chemo-photothermal eradication of plexiform neurofibromas.

4. Conclusions

Here, we developed homogeneous red-emitting carbon nanodots functionalized with discrete PEG chains exposing biotin groups at the surface (CDs-PEG-BT), exploited as potential active targeting agent towards plexiform neurofibroma type 1 (PN). The surface engineering approach enhanced optical and colloidal stability under physiological conditions, enabled efficient photothermal conversion of near-infrared light, and provided stable red emission, suitable for image-guided photothermal applications. The PEG shell also facilitated the adsorption of the poorly water-soluble mTOR inhibitor named sirolimus (5 %), which was demonstrated to be released on demand in a localized light-triggered manner. The CDs-PEG-BT@Sir conjugate showed in vitro selective cytotoxicity toward PN cell lines instead of normal human Schwann cells (HSC) mainly do to the controlled release of sirolimus and the ability of penetrating cancer NF1 cells. The CDs-PEG-BT@Sir demonstrated the ability to accumulate within complex 3D PN-in-a-dish spheroids, leading to enhanced chemo-photothermal eradication of the tumor mass at biocompatible power density (7 W cm^{-2}) under the guidance of fluorescence imaging.

In summary, the CDs-PEG-BT@Sir conjugate exhibits a unique combination of properties that position it well for the treatment of PN lesions. Its small size potentially facilitates enhanced extravasation and tissue distribution, while its bright fluorescence enables real-time imaging. The integration of light-responsive hyperthermia with on-demand drug release offers a powerful approach for precise and effective therapy, supporting its potential for clinical application. Some limitations remain, particularly in enabling fluorescence quantum yield and absorption within the NIR-I/II window to enhance imaging and therapeutic depth. Nevertheless, our findings provide a strong foundation for advancing surface-engineered nanoplatforms and addressing the unmet needs of rare diseases like NF1-associated PNs through innovative theranostic strategies.

Author statement

The manuscript was written through contributions of all authors.

All authors have given approval to the final version of the manuscript. M.M., writing original draft, editing, supervision, optimization of PN models; R.C., writing original draft, optimization of PN models, chemical characterization, data curation; M.V.G and A.C., writing original draft, optimization of PN models; A.M. and G.C., supervision, founding. D.V., conceived the project, writing original draft, editing, optimization of PN models; N.M., conceived the project, supervision, writing original draft, editing, research, data curation, founding.

CRediT authorship contribution statement

Marina Macchiaiolo: Funding acquisition, Data curation, Conceptualization. **Roberta Cillari:** Writing – original draft, Methodology, Investigation, Formal analysis, Data curation. **Michaela V. Gonfiantini:** Writing – review & editing, Visualization, Software. **Antonella Cacchione:** Writing – review & editing, Formal analysis. **Angela Mastronuzzi:** Writing – review & editing, Resources. **Gennara Cavallaro:** Writing – review & editing, Resources. **Davide Vecchio:** Writing – review & editing, Writing – original draft, Project administration, Formal analysis, Conceptualization. **Nicolò Mauro:** Writing – review & editing, Writing – original draft, Supervision, Project administration, Methodology, Funding acquisition, Formal analysis, Data curation, Conceptualization.

Declaration of competing interest

The authors declare that they have no known competing financial interests or personal relationships that could have appeared to influence the work reported in this paper.

Acknowledgments

This research has received funding from the European Union—NextGenerationEU through the Italian Ministry of University and Research under PNRR—M4C2-I1.3 Project PE_00000019: “Health

Extended Alliance for Innovative Therapies, Advanced Lab-research, and Integrated Approaches of Precision Medicine—HEAL ITALIA" to G.C. and N.M. CUP: B73C22001250006. The views and opinions expressed are those of the authors only and do not necessarily reflect those of the European Union or the European Commission. Neither the European Union nor the European Commission can be held responsible for them.

Supplementary materials

Supplementary material associated with this article can be found, in the online version, at doi:10.1016/j.surfin.2025.105978.

Data availability

No data was used for the research described in the article.

References

[1] V.M. Riccardi, Von Recklinghausen neurofibromatosis, N. Engl. J. Med. 305 (1981) 1617–1627, https://doi.org/10.1056/NEJM198112313052704.

[2] D.H. Gutmann, R.E. Ferner, R.H. Listernick, B.R. Korf, P.L. Wolters, K.J. Johnson, Neurofibromatosis type 1, Nat. Rev. Dis. Primers 3 (2017), https://doi.org/10.1038/NRDP.2017.4.

[3] K. Doser, E.W. Andersen, L. Kenborg, S.O. Dalton, J.R.M. Jepsen, A. Krøyer, J. Østergaard, H. Hove, S.A. Sørensen, C. Johansen, J. Mulvihill, J.F. Winther, P. E. Bidstrup, Clinical characteristics and quality of life, depression, and anxiety in adults with neurofibromatosis type 1: a nationwide study, Am. J. Med. Genet A 182 (2020) 1704–1715, https://doi.org/10.1002/AJMG.A.61627.

[4] E. Legius, L. Messiaen, P. Wolkenstein, P. Pancza, R.A. Avery, Y. Berman, J. Blakeley, D. Babovic-Vuksanovic, K.S. Cunha, R. Ferner, M.J. Fisher, J. M. Friedman, D.H. Gutmann, H. Kehrer-Sawatzki, B.R. Korf, V.F. Mautner, S. Peltonen, K.A. Rauen, V. Riccardi, E. Schorry, A. Stemmer-Rachamimov, D. A. Stevenson, G. Tadini, N.J. Ullrich, D. Viskochil, K. Wimmer, K. Yohay, A. Gomes, J.T. Jordan, V. Mautner, V.L. Merker, M.J. Smith, M. Anten, A. Aylsworth, D. Baralle, S. Barbarot, F. Barker, S. Ben-Shachar, A. Bergner, D. Bessis, I. Blanco, C. Cassiman, P. Ciavarelli, M. Clementi, T. Frébourg, M. Giovannini, D. Halliday, C. Hammond, C.O. Hanemann, H. Hanson, A. Heiberg, P. Joly, M. Kalamarides, M. Karajannis, D. Kroshinsky, M. Larralde, C. Lázaro, L. Le, M. Link, R. Listernick, M. MacCollin, C. Mallucci, C. Moertel, A. Mueller, J. Ngeow, R. Oostenbrink, R. Packer, L. Papi, A. Parry, J. Peltonen, D. Pichard, B. Poppe, N. Rezende, L. O. Rodrigues, T. Rosser, M. Ruggieri, E. Serra, V. Steinke-Lange, S.M. Stivaros, A. Taylor, J. Toelen, J. Tonsgard, E. Trevisson, M. Upadhyaya, A. Varan, M. Wilson, H. Wu, G. Zadeh, S.M. Huson, D.G. Evans, S.R. Plotkin, Revised diagnostic criteria for neurofibromatosis type 1 and Legius syndrome: an international consensus recommendation, Genet Med. 23 (2021) 1506–1513, https://doi.org/10.1038/S41436-021-01170-5.

[5] M. Macchiaiolo, F.M. Panfili, D. Vecchio, M.V. Gonfiantini, F. Cortellessa, C. Caciolo, M. Zollino, M. Accadia, M. Seri, M. Chinali, C. Mammì, M. Tartaglia, A. Bartuli, P. Alfieri, M. Priolo, A deep phenotyping experience: up to date in management and diagnosis of Malan syndrome in a single center surveillance report, Orphanet. J. Rare Dis 17 (2022), https://doi.org/10.1186/S13023-022-02384-9.

[6] K. Staser, F.C. Yang, D.W. Clapp, Pathogenesis of plexiform neurofibroma: tumor-stromal/hematopoietic interactions in tumor progression, Annu. Rev. Pathol. 7 (2012) 469–495, https://doi.org/10.1146/ANNUREV-PATHOL-011811-132441.

[7] A.M. Gross, G. Singh, S. Akshintala, A. Baldwin, E. Dombi, S. Ukwuani, A. Goodwin, D.J. Liewehr, S.M. Steinberg, B.C. Widemann, Association of plexiform neurofibroma volume changes and development of clinical morbidities in neurofibromatosis 1, Neuro Oncol. 20 (2018) 1643–1651, https://doi.org/10.1093/NEUONC/NOY067.

[8] B.C. Widemann, M.J. Fisher, E. Dombi, A. Cantor, S. Vinks, B. Korf, E. Schorry, D. Gutmann, R. Packer, B.D. Weiss, Phase II study of the mTOR inhibitor sirolimus for nonprogressive NF1-associated plexiform neurofibromas: a Neurofibromatosis Consortium study, J. Clin. Oncol. 28 (2010) e13601–e13602, https://doi.org/10.1200/JCO.2010.28.15_SUPPL.E13601.

[9] J.M. Hartinger, P. Ryšánek, O. Slanař, M. Šíma, Pharmacokinetic principles of dose adjustment of mTOR inhibitors in solid organ transplanted patients, J. Clin. Pharm. Ther. 47 (2022) 1362–1367, https://doi.org/10.1111/JCPT.13753.

[10] B. Weiss, B.C. Widemann, P. Wolters, E. Dombi, A.A. Vinks, A. Cantor, B. Korf, J. Perentesis, D.H. Gutmann, E. Schorry, R. Packer, M.J. Fisher, Sirolimus for non-progressive NF1-associated plexiform neurofibromas: an NF clinical trials consortium phase II study, Pediatr. Blood Cancer 61 (2014) 982–986, https://doi.org/10.1002/PBC.24873.

[11] A. Haeri, M. Osouli, F. Bayat, S. Alavi, S. Dadashzadeh, Nanomedicine approaches for sirolimus delivery: a review of pharmaceutical properties and preclinical studies, Artif. Cells Nanomed. Biotechnol. 46 (2018) 1–14, https://doi.org/10.1080/21691401.2017.1408123.

[12] J. JU, M. RH, Nanocrystal technology, drug delivery and clinical applications, Int. J. Nanomed. 3 (2008) 295, https://doi.org/10.2147/IJN.S595.

[13] Y. Dou, J. Guo, Y. Chen, S. Han, X. Xu, Q. Shi, Y. Jia, Y. Liu, Y. Deng, R. Wang, X. Li, J. Zhang, Sustained delivery by a cyclodextrin material-based nanocarrier potentiates antiatherosclerotic activity of rapamycin via selectively inhibiting mTORC1 in mice, J. Control Release 235 (2016) 48–62, https://doi.org/10.1016/J.JCONREL.2016.05.049.

[14] X. Pang, J. Wang, X. Tan, F. Guo, M. Lei, M. Ma, M. Yu, F. Tan, N. Li, Dual-modal imaging-guided theranostic nanocarriers based on indocyanine green and mTOR inhibitor rapamycin, ACS Appl. Mater. Interfaces 8 (2016) 13819–13829, https://doi.org/10.1021/ACSAMI.6B04010.

[15] Q. Zhao, Y. Zhang, T. Yu, J. Lu, G. Sun, X. Luo, S. Wang, Tailored nanoplatforms with detachable 'meteorolite' for photothermal-enhanced programmed tumor therapy, Carbon N Y 199 (2022) 119–131, https://doi.org/10.1016/J.CARBON.2022.07.073.

[16] C. Scialabba, A. Sciortino, F. Messina, G. Buscarino, M. Cannas, G. Roscigno, G. Condorelli, G. Cavallaro, G. Giammona, N. Mauro, Highly homogeneous biotinylated carbon nanodots: red-emitting nanoheaters as theranostic agents toward precision cancer medicine, ACS Appl. Mater Interfaces 11 (2019) 19854–19866, https://doi.org/10.1021/acsami.9b04925.

[17] B. Geng, D. Yang, D. Pan, L. Wang, F. Zheng, W. Shen, C. Zhang, X. Li, NIR-responsive carbon dots for efficient photothermal cancer therapy at low power densities, Carbon N Y (2018), https://doi.org/10.1016/j.carbon.2018.03.084.

[18] Y. Li, G. Bai, S. Zeng, J. Hao, Theranostic carbon dots with innovative NIR-II emission for in vivo renal-excreted optical imaging and photothermal therapy, ACS Appl. Mater Interfaces 11 (2019) 4737–4744, https://doi.org/10.1021/acsami.8b14877.

[19] N. Mauro, M.A. Utzeri, A. Sciortino, F. Messina, M. Cannas, R. Popescu, D. Gerthsen, G. Buscarino, G. Cavallaro, G. Giammona, Decagram-scale synthesis of multicolor carbon nanodots: self-tracking nanoheaters with inherent and selective anticancer properties, ACS Appl. Mater. Interfaces 14 (2022) 2551–2563, https://doi.org/10.1021/ACSAMI.1C19599/ASSET/IMAGES/LARGE/AM1C19599_0006.JPEG.

[20] N. Mauro, M.A. Utzeri, S.E. Drago, A. Nicosia, S. Costa, G. Cavallaro, G. Giammona, Hyaluronic acid dressing of hydrophobic carbon nanodots: a self-assembling strategy of hybrid nanocomposites with theranostic potential, Carbohydr. Polym. (2021), https://doi.org/10.1016/j.carbpol.2021.118213.

[21] N. Mauro, C. Scialabba, G. Cavallaro, M. Licciardi, G. Giammona, Biotin-containing reduced graphene oxide-based nanosystem as a multieffect anticancer agent: combining hyperthermia with targeted chemotherapy, Biomacromolecules 16 (2015) 2766–2775.

[22] D.N. Heo, D.H. Yang, H.J. Moon, J.B. Lee, M.S. Bae, S.C. Lee, W.J. Lee, I.C. Sun, I. K. Kwon, Gold nanoparticles surface-functionalized with paclitaxel drug and biotin receptor as theranostic agents for cancer therapy, Biomaterials 33 (2012) 856–866, https://doi.org/10.1016/j.biomaterials.2011.09.064.

[23] K. Vinothini, N.K. Rajendran, M.A. Munusamy, A.A. Alarfaj, M. Rajan, Development of biotin molecule targeted cancer cell drug delivery of doxorubicin loaded κ-carrageenan grafted graphene oxide nanocarrier, Mater. Sci. Eng. C (2019), https://doi.org/10.1016/j.msec.2019.03.011.

[24] F. Sedel, D. Bernard, D.M. Mock, A. Tourbah, Targeting demyelination and virtual hypoxia with high-dose biotin as a treatment for progressive multiple sclerosis, Neuropharmacology 110 (2016) 644–653, https://doi.org/10.1016/J.NEUROPHARM.2015.08.028.

[25] R.J.M. Franklin, C. Ffrench-Constant, Remyelination in the CNS: from biology to therapy, Nat. Rev. Neurosci. 9 (2008) 839–855, https://doi.org/10.1038/NRN2480.

[26] R. Spector, D. Mock, Biotin transport through the blood-brain barrier, J. Neurochem. 48 (1987) 400–404, https://doi.org/10.1111/J.1471-4159.1987.TB04107.X.

[27] M. Wiśniewski, J. Czarnecka, P. Bolibok, M. Świdziński, K. Roszek, New insight into the fluorescence quenching of nitrogen-containing carbonaceous quantum dots—From surface chemistry to biomedical applications, Materials 14 (2021) 2454, https://doi.org/10.3390/MA14092454, 2021, Vol. 14, Page 2454.

[28] Junli Wang, Yongzhen Yang, Xuguang Liu, Solid-state fluorescent carbon dots: quenching resistance strategies, high quantum efficiency control, multicolor tuning, and applications, Mater. Adv. 1 (2020) 3122–3142, https://doi.org/10.1039/D0MA00632G.

[29] N. Mauro, C. Scialabba, R. Puleio, P. Varvarà, M. Licciardi, G. Cavallaro, G. Giammona, SPIONs embedded in polyamino acid nanogels to synergistically treat tumor microenvironment and breast cancer cells, Int. J. Pharm. 555 (2019) 207–219, https://doi.org/10.1016/J.IJPHARM.2018.11.046.

[30] A. Madonia, G. Minervini, A. Terracina, A. Pramanik, V. Martorana, A. Sciortino, C. M. Carbonaro, C. Olla, T. Sibillano, C. Giannini, E. Fanizza, M.L. Curri, A. Panniello, F. Messina, M. Striccoli, Dye-derived red-emitting carbon dots for lasing and solid-State lighting, ACS Nano 17 (2023) 21274–21286, https://doi.org/10.1021/ACSNANO.3C05566/ASSET/IMAGES/LARGE/NN3C05566_0005.JPEG.

[31] H. Ding, X.X. Zhou, J.S. Wei, X.B. Li, B.T. Qin, X.B. Chen, H.M. Xiong, Carbon dots with red/near-infrared emissions and their intrinsic merits for biomedical applications, Carbon N Y 167 (2020) 322–344, https://doi.org/10.1016/j.carbon.2020.06.024.

[32] J. Ge, Q. Jia, W. Liu, L. Guo, Q. Liu, M. Lan, H. Zhang, X. Meng, P. Wang, Red-emissive carbon dots for fluorescent, photoacoustic, and thermal theranostics in living mice, Adv. Mater. 27 (2015) 4169–4177, https://doi.org/10.1002/adma.201500323.

[33] J. Ge, Q. Jia, W. Liu, L. Guo, Q. Liu, M. Lan, H. Zhang, X. Meng, P. Wang, Red-emissive carbon dots for fluorescent, photoacoustic, and thermal theranostics in living mice, Adv. Mater. (2015), https://doi.org/10.1002/adma.201500323.

[34] Z. Zhu, Y. Zhai, Z. Li, P. Zhu, S. Mao, C. Zhu, D. Du, L.A. Belfiore, J. Tang, Y. Lin, Red carbon dots: optical property regulations and applications, Mater. Today 30 (2019) 52–79, https://doi.org/10.1016/j.mattod.2019.05.003.

[35] M.L. Schipper, G. Iyer, A.L. Koh, Z. Cheng, Y. Ebenstein, A. Aharoni, S. Keren, L. A. Bentolila, J. Li, J. Rao, X. Chen, U. Banin, A.M. Wu, R. Sinclair, S. Weiss, S. S. Gambhir, Particle size, surface coating, and PEGylation influence the biodistribution of quantum dots in living mice, Small (2009), https://doi.org/10.1002/smll.200800003.

[36] X. Huang, F. Zhang, L. Zhu, K.Y. Choi, N. Guo, J. Guo, K. Tackett, P. Anilkumar, G. Liu, Q. Quan, H.S. Choi, G. Niu, Y.P. Sun, S. Lee, X. Chen, Effect of injection routes on the biodistribution, clearance, and tumor uptake of carbon dots, ACS Nano (2013), https://doi.org/10.1021/nn401911k.

[37] A. Sciortino, F. Ferrante, N. Mauro, G. Buscarino, L. Sciortino, G. Giammona, M. Cannas, D. Duca, F. Messina, Disclosing the emissive surface traps in green-emitting carbon nanodots, Carbon N Y 173 (2021) 454–461, https://doi.org/10.1016/j.carbon.2020.11.030.

[38] O.A. Savchuk, J.J. Carvajal, J. Massons, M. Aguiló, F. Díaz, Determination of photothermal conversion efficiency of graphene and graphene oxide through an integrating sphere method, Carbon N Y (2016), https://doi.org/10.1016/j.carbon.2016.02.075.

[39] J. Lu, L. Song, S. Feng, K. Wang, Y. Mao, Y. Gao, Q. Zhao, S. Wang, Nanozyme-mediated biocatalysis as a mitochondrial oxidative stress amplifier for tumor nanocatalytic immunotherapy, Chem. Eng. J. 481 (2024) 148270, https://doi.org/10.1016/J.CEJ.2023.148270.

[40] S. Sarkar, N. Levi-Polyachenko, Conjugated polymer nano-systems for hyperthermia, imaging and drug delivery, Adv. Drug Deliv. Rev. (2020), https://doi.org/10.1016/j.addr.2020.01.002.

[41] S.K. Sharma, N. Shrivastava, F. Rossi, L.D. Tung, N.T.K. Thanh, Nanoparticles-based magnetic and photo induced hyperthermia for cancer treatment, Nano Today 29 (2019) 100795, https://doi.org/10.1016/j.nantod.2019.100795.

[42] N. Mauro, M. Andrea Utzeri, A. Sciortino, M. Cannas, F. Messina, G. Cavallaro, G. Giammona, Printable thermo- and photo-stable poly(D,L-lactide)/carbon nanodots nanocomposites via heterophase melt-extrusion transesterification, Chem. Eng. J. 443 (2022) 136525, https://doi.org/10.1016/J.CEJ.2022.136525.

[43] P. Simamora, J.M. Alvarez, S.H. Yalkowsky, Solubilization of rapamycin, Int. J. Pharm. 213 (2001) 25–29, https://doi.org/10.1016/S0378-5173(00)00617-7.

[44] S.A. Jadhav, A.J. Raval, A.B. Jariwala, C.B. Engineer, V.B. Patravale, Sirolimus micro/nano particles coated drug-eluting stents using QbD paradigm: potential approach for the amelioration of arterial diseases, J. Drug Deliv. Sci. Technol. 95 (2024) 105629, https://doi.org/10.1016/J.JDDST.2024.105629.

[45] K. Wang, Y. Du, Z. Zhang, K. He, Z. Cheng, L. Yin, D. Dong, C. Li, W. Li, Z. Hu, C. Zhang, H. Hui, C. Chi, J. Tian, Fluorescence image-guided tumour surgery, Nature Rev. Bioeng. 3 (1) (2023) 161–179, https://doi.org/10.1038/s44222-022-00017-1, 2023 1.

[46] M. Vedhanayagam, I.S. Raja, A. Molkenova, T.S. Atabaev, K.J. Sreeram, D.W. Han, Carbon dots-mediated fluorescent scaffolds: recent trends in image-guided tissue engineering applications, Int. J. Mol. Sci. 22 (2021) 5378, https://doi.org/10.3390/IJMS22105378, 2021, Vol. 22, Page 5378.

[47] W. Miao, G. Shim, G. Kim, S. Lee, H.J. Lee, Y.B. Kim, Y. Byun, Y.K. Oh, Image-guided synergistic photothermal therapy using photoresponsive imaging agent-loaded graphene-based nanosheets, J. Control. Rel. 211 (2015) 28–36, https://doi.org/10.1016/j.jconrel.2015.05.280.

[48] A. Nicosia, G. Cavallaro, S. Costa, M.A. Utzeri, A. Cuttitta, G. Giammona, N. Mauro, Carbon nanodots for on demand chemophotothermal therapy combination to elicit necroptosis: overcoming apoptosis resistance in breast cancer cell lines, Cancers (Basel) (2020), https://doi.org/10.3390/cancers12113114.

[49] B.N. Somatilaka, A. Sadek, R.M. McKay, L.Q. Le, Malignant peripheral nerve sheath tumor: models, biology, and translation, Oncogene 41 (2022) 2405–2421, https://doi.org/10.1038/S41388-022-02290-1.

[50] J.M. Kraniak, A. Chalasani, M.R. Wallace, R.R. Mattingly, Development of 3D culture models of plexiform neurofibroma and initial application for phenotypic characterization and drug screening, Exp. Neurol. 299 (2017) 289, https://doi.org/10.1016/J.EXPNEUROL.2017.10.012.

[51] J.M. Kraniak, A. Chalasani, M.R. Wallace, R.R. Mattingly, Development of 3D culture models of plexiform neurofibroma and initial application for phenotypic characterization and drug screening, Exp. Neurol. 299 (2018) 289–298, https://doi.org/10.1016/J.EXPNEUROL.2017.10.012.

[52] V. Roy, B. Magne, M. Vaillancourt-Audet, M. Blais, S. Chabaud, E. Grammond, L. Piquet, J. Fradette, I. Laverdière, V.J. Moulin, S. Landreville, L. Germain, F. A. Auger, F. Gros-Louis, S. Bolduc, Human organ-specific 3D cancer models produced by the stromal self-assembly method of tissue engineering for the study of solid tumors, Biomed. Res. Int. 2020 (2020), https://doi.org/10.1155/2020/6051210.

[53] J. Radhakrishnan, S. Varadaraj, S.K. Dash, A. Sharma, R.S. Verma, Organotypic cancer tissue models for drug screening: 3D constructs, bioprinting and microfluidic chips, Drug Discov. Today 25 (2020) 879–890, https://doi.org/10.1016/j.drudis.2020.03.002.

[54] J.M. Kraniak, A. Chalasani, M.R. Wallace, R.R. Mattingly, Development of 3D culture models of plexiform neurofibroma and initial application for phenotypic characterization and drug screening, Exp. Neurol. 299 (2018) 289–298, https://doi.org/10.1016/J.EXPNEUROL.2017.10.012.

[55] I.A. Khawar, J.H. Kim, H.-J. Kuh, Improving drug delivery to solid tumors: priming the tumor microenvironment, J. Control. Release 201 (2015) 78–89, https://doi.org/10.1016/j.jconrel.2014.12.018.

[56] H.A. Goubran, R.R. Kotb, J. Stakiw, M.E. Emara, T. Burnouf, Regulation of tumor growth and metastasis: the role of tumor microenvironment, Cancer Growth Met. 7 (2014) 9–18, https://doi.org/10.4137/CGM.S11285.

[57] N. Mauro, C. Scialabba, R. Puleio, P. Varvarà, M. Licciardi, G. Cavallaro, G. Giammona, SPIONs embedded in polyamino acid nanogels to synergistically treat tumor microenvironment and breast cancer cells, Int. J. Pharm. 555 (2019) 207–219, https://doi.org/10.1016/J.IJPHARM.2018.11.046.